

# Accelerated Deep Learning Dynamics for Atomic Layer Deposition of Al(Me)<sub>3</sub> and Water on OH/Si(111)

Hiroya Nakata,\* Michael Filatov(Gulak),\* and Cheol Ho Choi\*



Cite This: *ACS Appl. Mater. Interfaces* 2022, 14, 26116–26127



Read Online

ACCESS |

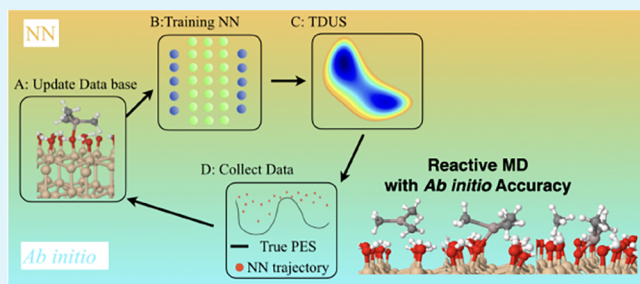
Metrics & More

Article Recommendations

Supporting Information

**ABSTRACT:** Knowledge of the detailed mechanism behind the atomic layer deposition (ALD) can greatly facilitate the optimization of the manufacturing process. Computational modeling can potentially foster the understanding; however, the presently available capabilities of the accurate *ab initio* computational techniques preclude their application to modeling surface processes occurring on a long time scale, such as ALD. Although the situation can be greatly improved using machine learning (ML), this technique requires an enormous amount of data for training datasets. Here, we propose an iterative protocol for optimizing ML training datasets and apply ML-assisted *ab initio* calculations to model surface reactions occurring during the Al(Me)<sub>3</sub>/H<sub>2</sub>O ALD process on the OH-terminated Si (111) surface. The protocol uses a recently developed low-dimensional projection technique (TDUS), greatly reducing the amount of information required to achieve high accuracy (*ca.* 1 kcal/mol or less) of the developed ML models. The resulting free energy landscapes reveal fine details of various aspects of the target ALD process, such as the surface proton transfer, zwitterionic surface configurations, elimination–addition/addition–elimination, and S<sub>N</sub>2 reactions as well as the role of the surface entropic and temperature effects. Simulations of adsorption dynamics predict that the maximum physisorption rate of *ca.* 70% is achieved at the incidence velocity *v*<sub>rms</sub> of the reactants in the range of 15–20 Å/ps. Hence, the proposed protocol furnishes a very effective tool to study complex chemical reaction dynamics at a much reduced computational cost.

**KEYWORDS:** machine learning, reaction coordinate projection, atomic layer deposition, Al(Me)<sub>3</sub>, silicon surface, deep MD



## INTRODUCTION

The atomic layer deposition (ALD) process<sup>1–4</sup> has become an indispensable tool for the manufacturing of nanoscale semiconductor devices<sup>5</sup> as it allows the deposition of conformal layers on the surface of a substrate with precise thickness control up to the nanometer scale. During the process, the substrate surface is sequentially exposed to deposition of vapors of precursor compounds in alternating non-overlapping pulses interlaced, if necessary, by pulses of an inert gas. The respective chemical reactions in the ALD cycle are complementary and self-terminating, which allows growth of layers of perfectly controllable thickness on substrates of an arbitrarily complex shape.

Aluminum oxide has become<sup>6</sup> an important alternative to silica (SiO<sub>2</sub>) commonly used as a gate dielectric, as it possesses a number of desirable characteristics, such as a large band gap ( $\kappa$  of ~9 eV), high dielectric constant ( $\kappa$  of ~9), and large breakdown voltage (5–10 MV/cm).<sup>7–9</sup> Various aluminum halide, alkyl, and alkoxide precursors<sup>10–14</sup> have been used in combination with various oxygen sources for growing Al<sub>2</sub>O<sub>3</sub> thin films of high quality at reduced temperatures, in both ALD and CVD (chemical vapor deposition) processes. The initial experimental and theoretical mechanistic studies<sup>11,15–22</sup> estab-

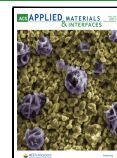
lished that the OH-terminated Si surface is more reactive than the H-terminated surface and that the Al<sub>2</sub>O<sub>3</sub> films grown on the former surface have a much smoother morphology than those grown on the latter surface. In addition, as a result of the CH<sub>4</sub> release reactions, not only simple mono-dentate but also bi- or even tridentate interfacial Al–O structures were predicted,<sup>19</sup> see also structures in Figure 2.

Sophisticated modeling of the deposition efficiency has been employed to minimize waste and to study temperature and time-dependent surface morphology. The modeling included various factors, such as subsequent surface reactions, deposition rates, and backward reactions.<sup>23</sup> Experimentally, gaseous HOAl(CH<sub>3</sub>)<sub>2</sub> was observed as a secondary reaction product during the water pulse, which was assigned to the desorption of the initial surface products during the ALD process.<sup>24</sup>

Received: January 28, 2022

Accepted: May 11, 2022

Published: May 24, 2022



In addition to the operando spectroscopic analyses,<sup>25,26</sup> *ab initio* studies of the static structures and mathematical modeling of the reaction rates have paved a way for the fundamental understanding of the surface chemical reactions. However, the actual surface phenomena may differ from the static picture because the temperature-dependent reaction dynamics may follow reaction pathways that deviate from the adiabatic minimum energy paths. In such a case, molecular dynamics simulations on the *ab initio* potential energy surfaces are indispensable to properly describe the detailed mechanism of the pertinent chemical reactions. However, such modeling seems to be much too computationally demanding.

To overcome these challenges, molecular dynamics simulations assisted by machine learning (ML) techniques seem to be useful. Recently, adaptation of machine learning techniques to the scientific computations has become a popular activity. Several successful applications of the Behler–Parrinello neural network (BPNN),<sup>27</sup> the Gaussian approximation potential (GAP),<sup>28</sup> the gradient domain machine learning (GDML),<sup>29</sup> and the recent deep potential for molecular dynamics (DeePMD)<sup>30,31</sup> methods have been reported. These developments promise MD simulations with an accuracy comparable to density functional theory methods, while keeping the cost at a level of the classical MD based on empirical potentials.

Although the ML approach is potentially promising, a particular challenge is the large amount of data required to achieve the high accuracy of the models. Often, many thousands or even millions of atomic configurations are used as training datasets for ML models. Therefore, collecting the data points that are the most relevant for the particular purpose is crucial to successful utilization of the ML potential.

A similar situation arises in the case of molecular dynamic simulations, which require proper sampling to construct the free energy surfaces. This is especially challenging for *ab initio* molecular dynamics because typical configurational transitions or chemical reactions occur on time scales that are significantly longer than those accessible using the standard *ab initio* molecular dynamics methodologies.

In the context of *ab initio* molecular dynamics, the two most popular contemporary free energy methods are umbrella sampling<sup>32–38</sup> and metadynamics.<sup>39–41</sup> The successful application of these enhanced sampling techniques is dependent on the appropriate definition of the reaction coordinate, or a set of collective variables, which requires, at least, some *a priori* understanding of the underlying reaction pathways.

The collective variables approach has been extremely successful due to its ability to sample large regions of the configurational space. In addition, no assumptions are made about the final state. However, it is usually difficult to define a set of collective variables, which can take into account the entire relevant configurational space, especially in the case of large systems. In such cases, the number of collective variables becomes too large, requiring a significant computational effort. Additionally, the interpretation of the configurational space becomes cumbersome.

Recently, a one-dimensional projection (ODP) technique was introduced to overcome the challenges of multidimensional sampling.<sup>35,42</sup> With the help of a projected “advancement of reaction” ( $\xi$ ) control parameter, it was demonstrated that multidimensional sampling could be performed using a single parameter only, thus dramatically reducing the computational overhead. Its two-dimensional extension with umbrella sampling (TDUS) has been used successfully for the efficient sampling of

complex and sophisticated molecular recognition and polymer aggregation reactions.<sup>43</sup>

In the context of obtaining the most relevant data for training ML potentials, the same techniques (ODP and TDUS) can also be effective. One of the main goals of this study is to examine these sampling techniques in the context of ML training. Using the Al(CH<sub>3</sub>)<sub>3</sub>/H<sub>2</sub>O ALD process<sup>6</sup> as an example, the resulting ML potentials enable obtaining the free energy landscapes of multiple interfacial adsorption chemical reactions in a broad range of temperatures, potentially revealing previously unknown metastable intermediates. Using the same ML potentials, the reaction dynamics of the initial adsorption processes has been simulated, which described the temperature-dependent adsorption processes on an ultrafast time scale and yielded the respective distributions of the initial surface products with atomistic detail.

## ■ COLLECTIVE VARIABLE PROJECTION BY TDUS

One of the most important requirements for successful sampling is the correct definition of the reaction coordinates (Figure 1).

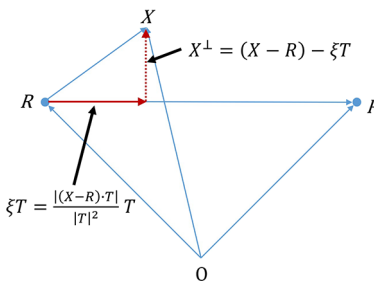


Figure 1. Definition of parameters in the TDUS algorithm.

Even if the reactant **R** and product **P** are well-known, defining a reaction coordinate between the two minima is challenging. This is because any point on the potential energy surfaces requires the exact structural information on all the vibrational degrees of freedom. However, a great advantage of the free energy surfaces before the potential energy surfaces is that the former are defined by the local probabilities of the occurrence of various structures. Therefore, only a handful of reaction coordinates (collective variables) are needed as control parameters, as long as the control parameters can faithfully connect the reactant **R** and the product **P**. Consequently, a chord vector **T** and the (dimensionless) advancement of the reaction parameter  $\xi$  can be defined as

$$\mathbf{T} = \mathbf{P} - \mathbf{R} \quad (1)$$

$$\xi = \frac{|(\mathbf{X} - \mathbf{R}) \cdot \mathbf{T}|}{|\mathbf{T}|^2} \quad (2)$$

where **P**, **R**, and **X** are the final, initial, and intermediate geometries of the target molecule, respectively. Again, it should be emphasized that these vectors are a subset of the entire geometry set, which can be represented by either the Cartesian, the internal, or the distance matrix coordinates, describing the system geometries. The transverse direction ( $X^\perp$ ) to the chord vector **T** and the (dimensionless) parameter ( $x_\perp$ ) can be defined as

$$\mathbf{X}^\perp = (\mathbf{X} - \mathbf{R}) - \xi \mathbf{T} \quad (3)$$

$$x_{\perp} = \frac{|X^{\perp}|}{|\mathbf{T}|} \quad (4)$$

By constraining the geometry along the transverse direction  $x_{\perp}$  as well as the reaction coordinate  $\xi$ , one can gain a wider range of sampling geometries, which provides a reliable training dataset of the reference configurations for ML. This particular 2D sampling procedure along both  $\xi$  and  $x_{\perp}$  is termed two-dimensional umbrella sampling (TDUS) and has been implemented<sup>43</sup> in the LAMMPS software.<sup>44</sup>

In the  $\xi$  and  $x_{\perp}$  space, TDUS can be performed using the following bias potentials

$$U_{\text{umb}}^i = \frac{1}{2} w_{\xi} (\xi - u_{\xi}^i)^2 \quad (5)$$

$$U_{\text{umb}}^{\perp,j} = \frac{1}{2} w_{\perp} (x_{\perp} - u_{\perp}^j)^2 \quad (6)$$

where  $U_{\text{umb}}^i$  and  $U_{\text{umb}}^{\perp,j}$  are the bias longitudinal and transverse potentials at the  $i$  and  $j$ th window. While  $w_{\xi}$  and  $w_{\perp}$  are the harmonic force constants,  $u_{\xi}^i$  and  $u_{\perp}^j$  define the  $(i, j)$ th 2D windows. For example, in the case of simulation of the reaction from Figure 2a,b, one has to include at least four different

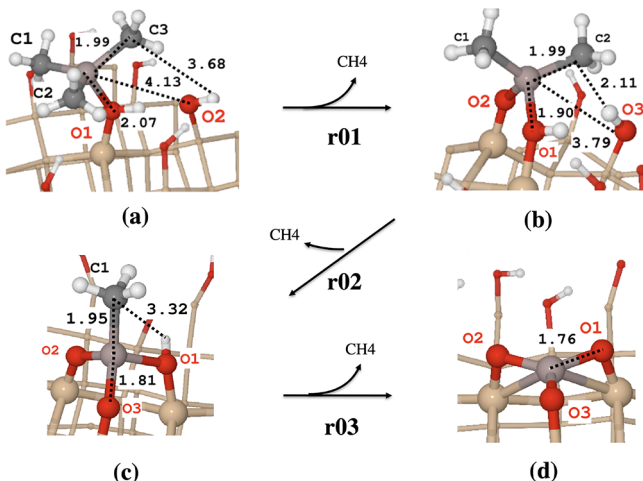


**Figure 2.** Surface chemical reactions of TMA on the (111)-Si surface: (a) Chemisorbed Al attaches to the surface with one Al–O bond, (b) Al with two Al–O bonds and the first CH<sub>4</sub> release, (c) Al with three Al–O bonds and the second CH<sub>4</sub> release, and (d) Al with three Al–O bonds and the third CH<sub>4</sub> release.

collective variables per each bond (Al–O, C–Al, C–H, and H–O), which results in a high computational cost even when using an MD approach based on ML, so that the evaluation of the free energy surfaces becomes difficult.

To generate the reference configuration dataset, *ab initio* simulations were performed using the SIESTA density functional theory program.<sup>45–47</sup> All the calculations employed the Perdew–Burke–Ernzerhof (PBE) functional<sup>48,49</sup> and the norm-conserving pseudopotential.<sup>50</sup> The energy cutoff was set at 250.0 Ry. The  $k$ -point sampling used the Monkhorst–Pack method<sup>51</sup> with  $2 \times 2 \times 1$  grids. To train the neural network potential and perform MD simulations, the DeePMDS kit package<sup>31</sup> was used, which was interfaced with the two-dimensional umbrella sampling method (TDUS) implemented in LAMMPS software.<sup>44</sup> For the neural network potential, five hidden layers were used and the number of neurons per layer was 240, 240, 120, 60, and 30.

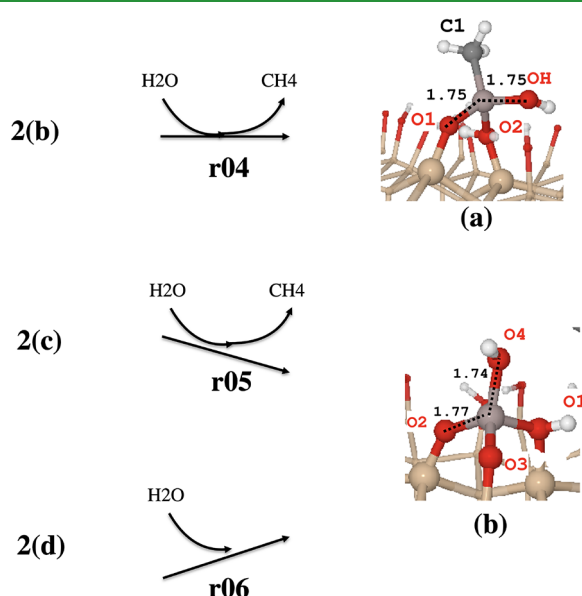
For production runs of the free energy sampling using ML potentials, TDUS along the  $\xi$  and the chord vector distance  $x_{\perp}$  was performed with the windows of 24 and 25 sampling points, respectively. As a result, the NVT simulations of 480 independent trajectories were performed for 6 ps to obtain the respective free energy surfaces of the surface reactions. MD simulations were performed with the Nose–Hoover thermostat,<sup>52,53</sup> and the velocity Verlet integrator was used for time integration with the time step of 0.5 fs.

Finally, we have investigated the initial TMA contact dynamics on the surface of (111) Si. As for the model cases, we have performed 1000 independent MD simulations, in which the initial TMA position and orientation were different from each other. By statistical analysis of the 1000 MD trajectories, we have investigated how initial contact affects the kinetics of the TMA surface reactions, within the range of velocities of 3–30 Å/ps.

## ■ TRAINING DEEP LEARNING POTENTIALS WITH TDUS

**TDUS Sampling over Six Reaction Paths.** As discussed above, the accuracy of ML potentials depends on the reference data, which must be the most relevant set of configurations for the given chemical process. The ALD process comprises various types of chemical reactions, such as initial adsorption and subsequent surface chemical reactions, which require dramatically different configurations to be included in the training dataset.

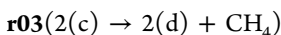
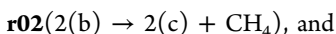
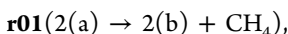
In this study, the ALD chemical reactions of the TMA (Al(Me)<sub>3</sub>) and H<sub>2</sub>O precursors on the (111)-Si surface capped with OH are investigated. Although the OH(111)-Si is well defined, multiple surface products may be produced upon the adsorption of TMA and H<sub>2</sub>O, as observed in the previous *ab initio* studies (see Figures 2 and 3). To accommodate various surface products, a Si<sub>96</sub>O<sub>32</sub>H<sub>32</sub> surface model with periodic boundary conditions and 32 capping OH-groups in the unit cell was set up.



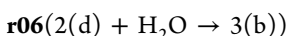
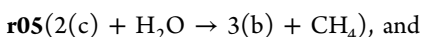
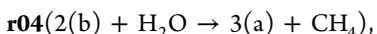
**Figure 3.** Surface chemical reactions of water on the (111)-Si surface: (a) water replacing CH<sub>4</sub> from structure 2(b), (b) water replacing CH<sub>4</sub> from structure 2(c), and water attached to Al from structure 2(d).

Figure 2 shows the surface products formed at different stages of the surface reactions, which are adopted for training in ML. The initial chemisorbed TMA on the surface O1 in Figure 2a shows an already formed Al–O1 interfacial bond with a length of 2.07 Å, which is consistent with the previous results *ab initio* of 2.02–2.046 Å.<sup>54,55</sup> All three Al–Me bonds as well as the O1–H bond are still intact. The abstraction of H (in O2) by C3 produces the second interfacial Al–O2 bond with the release of a methane in Figure 2b. Similarly, the H abstraction (on the O3) by C2 produces the third interfacial Al–O3 bond with the release of another methane in Figure 2c. Finally, the remaining methyl (C1) is desorbed from the surface through H abstraction at the O1 site. Previously, the first three structures were predicted by *ab initio* calculations performed on the surface of OH/Si(100)-2X1.<sup>19,54</sup> The structure in Figure 2d has not been previously predicted.

These four products may occur during the TMA deposition half cycle. They can represent a wide variety of potential energy regions, which is an important prerequisite to produce the most relevant yet diverse (nonredundant) data for ML training. For ML training, the structures between the four sites are obtained by defining three reaction paths:



The surface products formed by water absorption on the three structures in Figure 2b–d were also included in the ML training set, as shown in Figure 3a,b. These products can occur during the water deposition half cycle. Oxygen of the incoming water can nucleophilically attack Al by transferring its H to C2, which produces a hydroxyl group on Al with a leaving methane as shown in Figure 3a. The same nucleophilic attack in Figure 2c substitutes the methyl with the hydroxyl group, as shown in 3(b). Since there is no methyl group in Figure 2d, the incoming water is simply split into a hydroxyl group on Al and H on O1, producing a structure identical to 3(b). The intermediate structures for ML training are obtained along the following water absorption paths:



The configurational sampling over the six reaction paths (**r01**–**r06**) was performed using TDUS (two-dimensional umbrella sampling) to obtain the reference dataset for training the neural network force field. The structures before and after each reaction were used as the reactant and product when defining the “advancement of reaction”  $\xi$  control parameter for each reaction path. The reaction coordinates of the respective reactions were defined using the following bond lengths: For the CH<sub>4</sub> evolution, the bond formation of Al–O, C–H, and the bond dissociation of O–H and C–Al were used. For the water splitting reactions, the bond formation of water oxygen and aluminum, C and H, and bond dissociation of Al–C and H–O were used. Detailed definition of the reaction coordinates is provided in the Supporting Information. In order to ensure the optimum number of reference training data points, an iterative process described in the next section was utilized.

## Iterative Training Procedure Using the Free Energy Surface.

The neural network potential was constructed using the deep potential MD methodology (DeePM) recently developed by Zhang et al.<sup>30</sup> and Wang et al.<sup>31</sup> where the total energy  $E$  of the system is decomposed into the sum of the respective atomic energies. For many surface and chemical reactions, this approach was able to accurately reproduce the potential energy surfaces obtained in *ab initio* computations.<sup>56–60</sup> Although the previous studies pioneered the application of the neural network potentials to chemical reactions, they were limited to relatively simple proton transfer reactions or focused on the reaction product only. This was caused by the difficulty of defining the relevant reaction path of complex chemical reactions and of obtaining corresponding structural data along the paths for ML training. In this study, we propose an efficient and straightforward approach to these technologically difficult situations.

The parameters of the neural network potentials are iteratively trained as shown in Figure 4. First, the initial reference

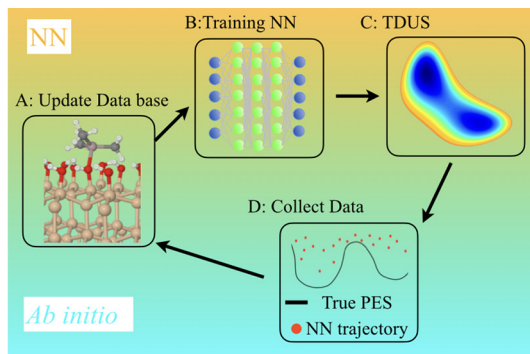


**Figure 4.** Schematic illustration of training of the neural network potential.

configurations are prepared by a small-scale *ab initio* MD simulation and a NEB (nudged elastic band) simulation over the six reaction paths shown in Figure 2. After updating the preliminary neural network potential (B in Figure 4), DeePM with TDUS is performed to simulate the free energy surfaces (free energy surfaces) of the six reaction paths (C). Step C generates a new set of geometric configurations. The initially prepared set of 10,000 configurations is gradually extended to *ca.* 100,000, *ab initio* calculations are performed for the new configurations (D), and they are added to the set of training data (A). The enlarged dataset is again utilized to train the neural network potentials (B), until the predicted free energy surfaces over all six reaction paths converge (C).

The described iterative procedure reduces the computational demands by 2–3 orders of magnitude. For the above example of neural network potential training, in total, 639,400 *ab initio* computations were performed, whereas the production molecular dynamics runs required computations at 70,044,000 points. Therefore, training of the neural network potentials required less than 1% ( $N_{\text{ab initio}}/N_{\text{MD}} = 0.00912$ ) of the number of calculations required for the production molecular dynamic (MD) runs.

**Validation of NN Models.** To validate the trained neural network model, the energies predicted by ML are compared with the *ab initio* energies shown in Figures S1a–c, where it is seen that the optimized neural network model can successfully reproduce energies within a wide range of values (−29239.6 to

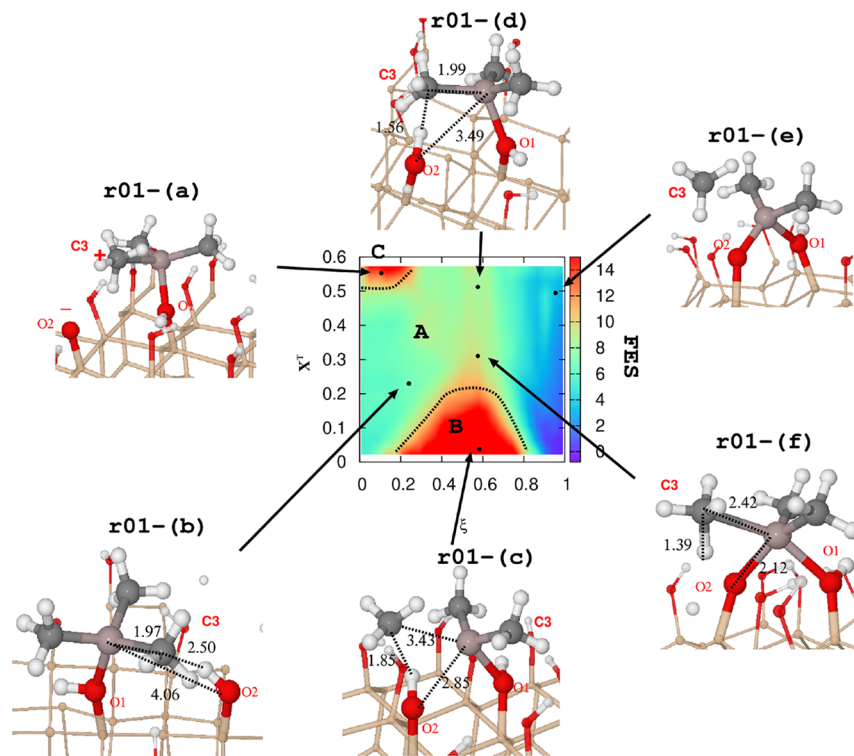


**Figure 5.** Two-dimensional free energy surface (FES) along reaction **r01** as obtained by neural net potential at 300 K. The corresponding structures in particular regions also have some important bond lengths in Å. The  $\xi$  and  $x_{\perp}$  are in Å, while free energy surfaces are in kcal/mol.

–27172.3 eV) with an overall RMSE (root mean square error) of 0.82 meV/atom ( $\sim$ 0.02 kcal/mol/atom) for the test dataset and 0.096 meV/atom ( $\sim$ 0.002 kcal/mol/atom) for the training dataset.

The convergence of the free-energy RMSE along the ML training iterations is shown in Figure S2, where it is seen that after only six iterations, the RMSE of the free-energy differences falls below 1.0 kcal/mol.

## RESULTS AND DISCUSSION

**Methane Desorption.** Free energy surfaces of the three  $\text{CH}_4$  evolution reactions (**r01–r03**) obtained by ML-TDUS (machine learning-two-dimensional umbrella sampling) at 300 K are shown in Figures 5–7 along with a number of important configurations, where  $\xi$  and  $x_{\perp}$  represent the “advancement of reaction” parameter and the direction transverse to the reaction vector  $\mathbf{T}$ . As  $\xi$  is a single degree of freedom, the  $x_{\perp}$  coordinate comprises the rest of the vibrational degrees of freedom. Therefore, the latter represents all the geometric changes other than the direction of the chemical reaction. The “advancement of reaction” parameter  $\xi$ , eq 2, is constrained to the domain  $\xi \in [0,1]$ , where 0 corresponds to the reactant and 1 to the product of the reaction. The value of  $x_{\perp}$  represents the degree of deviation from the direct reaction path.

To better understand free energy surfaces of the **r01** reaction, a number of representative geometries are shown in Figure 5. The reaction **r01** describes the desorption of a single methane molecule from the chemisorbed  $\text{AlMe}_3$  formed by abstracting a surface H atom from the OH group at the O2 position. As the free energies of regions B and C are much too high, the reaction proceeds through a relatively flat region A with shallow barriers exemplified by either **r01-(d)** and **r01-(f)** structures, which eventually produce the final product **r01-(e)**.

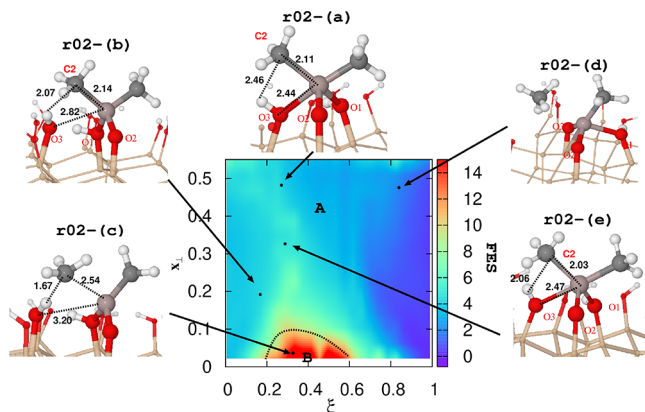


**Figure 6.** Two-dimensional free energy surface (FES) along reaction **r02** as obtained by neural net potential at 300 K. The corresponding structures in particular regions also have some important bond lengths in Å. The  $\xi$  and  $x_{\perp}$  are in Å, while free energy surfaces are in kcal/mol.

One of the structures in area A is **r01-(b)**, where the  $\text{C}3-\text{H}(\text{O}2)$  distance is reduced by 1.18 Å as compared to the reactant (see Figure 2a). Therefore, the flat part of the A area represents a simple internal rotation of  $\text{O}2-\text{H}$  or adsorbed  $\text{Al}(\text{CH}_4)_3$  with respect to the surface. The shallow reaction barriers of **r01-(d)** and **r01-(f)** represent different stages of an  $\text{S}_{\text{N}}2$ -type reaction; while the former is reactant-like, the latter is closer to the product. This is because two out of the three important distances in **r01-(d)** ( $\text{Al}-\text{O}2$ ,  $\text{H}(\text{O}2)-\text{C}3$ , and  $\text{Al}-\text{C}3$  are 3.49, 1.56, and 1.99 Å, respectively) are close to those of the reactant (4.13, 3.68, and 1.99 Å, respectively). On the other hand, those of **r01-(f)** represent product-like values of 2.12, 1.39, and 2.42 Å, respectively, with the secondary interfacial  $\text{Al}-\text{O}2$  bond.

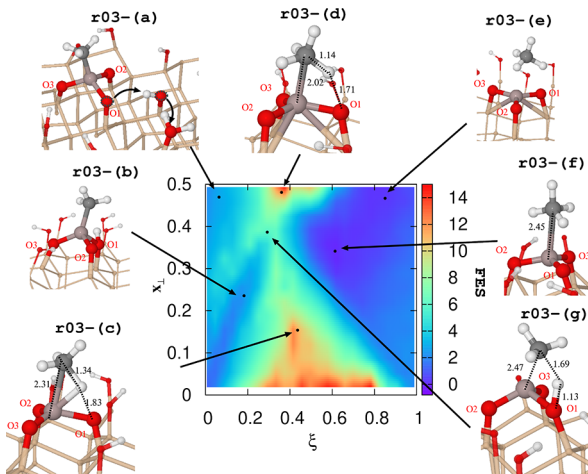


**Figure 7.** Two-dimensional free energy surface (FES) along reaction **r03** as obtained by neural net potential at 300 K. The corresponding structures in particular regions also have some important bond lengths in Å. The  $\xi$  and  $x_{\perp}$  are in Å, while free energy surfaces are in kcal/mol.

According to these values, the major change between the two structures occurs in the  $\text{H}(\text{O}_2)$ –C3 distance and it corresponds to the re-orientation of the surface hydroxyl group and the methyl group of  $\text{AlMe}_3$ . The high energy region B exemplified by **r01-(c)** represents a methyl radical leaving because the  $\text{H}(\text{O}_2)$ –C3 bond is not completely formed (1.85 Å), while the Al–C3 bond is almost broken (3.43 Å). In region C, exemplified by structure **r01-(a)**, formation of a pentacoordinated and positively charged C3 occurs by abstraction of the surface  $\text{H}(\text{O}_2)$ , which produces an interesting zwitterionic surface species (a negative O2 and a positive C3).

Overall, the unfavorable regions B and C represent elimination–addition- and addition–elimination-types of reactions, respectively, where the formation of highly unfavorable radical and zwitterionic species takes place. On the other hand, the preferred reaction region A exhibits the  $\text{S}_{\text{N}}2$ -type reactions, although a broad variation in terms of detailed structures is present.

For reaction **r02**, the free energy surfaces and important geometries are shown in Figure 6. Reaction **r02** introduces one more interfacial Al–O3 bond (**r02-(d)**) in the product of reaction **r01**. Compared to **r01**, the two surface Al–O bonds already present in the reactant prevent it from rotating along the Al–O bond. Nevertheless, a flat and shallow free surface area A is seen, which is characterized by a range of  $\text{H}(\text{O}_3)$ –C2 (2.07–2.46 Å) and Al–O3 (2.44–2.83 Å) distances as exemplified by **r02-(a)**, (b), and (e). The Al–O3 distance is considerably shortened from its value in the reactant (3.79 Å). On the other hand, the Al–C2 bond undergoes a minor variation (2.03–2.14 Å), which is in a close proximity to the corresponding value in the reactant (1.99 Å). The shortening of the Al–O3 bond by ca. 1 Å with respect to the reactant implies that the surface O3 is nucleophilically attacking Al in an  $\text{S}_{\text{N}}2$  fashion.

On the other hand, the structure **r02-(c)** in the high energy area B shows much more elongated Al–C2 (2.54 Å) and shortened C2–H(O3) (1.67 Å) bond lengths, while the Al–O3 bond is longer (3.20 Å) as compared to **r02-(a)**, (b), and (e). Although they all represent  $\text{S}_{\text{N}}2$ -type reactions, **r02-(a)**, (b), and (e) display characteristics of a nucleophilic attack, while **r02-(c)** corresponds to the elimination of methane by abstracting surface H.

Reaction **r03** in Figure 7 corresponds to methane desorption (**r03-(e)**) from the product of the reaction **r02** and proceeds without creating additional interfacial Al–O bonds. In contrast to the previous two reaction paths, two distinctive stable regions near **r03-(a)** and **r03-(b)** are seen on the reactant side. Similarly, the two most stable regions near **r03-(e)** (methane desorption) and **r03-(f)** (methane physisorption) are seen on the product side. Interestingly, **r03-(a)** represents a surface proton hopping, which produces a water molecule and a negatively charged O1 oxygen. Therefore, this particular surface state exhibits a chance of water desorption from the surface by a facile surface proton transfer, which has never been suggested before. On the other hand, **r03-(b)** still represents a reactant-like structure. Both **r03-(a)** and **r03-(b)** proceed further over a shallow transition state **r03-(g)**, where the Al–C bond is broken (2.47 Å) and the C–H(O1) bond is formed. This transition state leads to stable **r03-(f)**, where the methane molecule that leaves is physisorbed on the surface. The corresponding Al–C distance is 2.45 Å, which is even slightly shorter than in the transition state **r03-(g)** (2.47 Å). Obviously, the desorption of methane in **r03-(e)** is favorable on the free energy surface. However, the fact that **r03-(f)** is nearly as stable as **r03-(e)** indicates that the physisorbed methane in **r03-(f)** can be an important intermediate during the overall chemical reaction.

**Water Adsorption.** After the  $\text{AlMe}_3$  precursor pulse, it is important to understand the effect of the consecutive water adsorption on the Al precursor terminated surface. As shown in the **r04**, **r05**, and **r06** paths in Figure 3, the free energy surfaces of a single water adsorption on the respective surface products have been studied by ML-TDUS (ML two-dimensional umbrella sampling) and are shown in Figures 8–10, respectively.

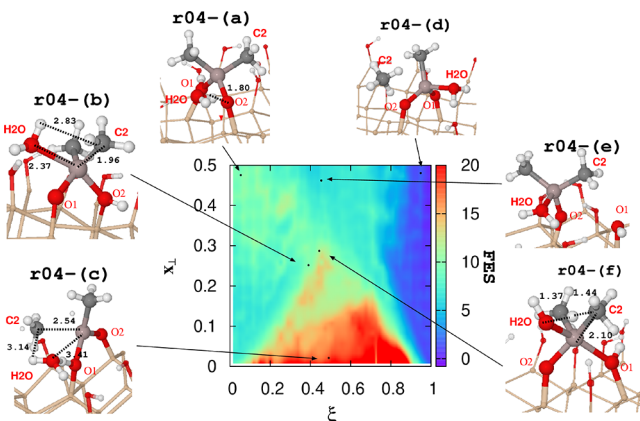


**Figure 8.** Two-dimensional free energy surface (FES) along reaction **r04** as obtained by neural net potential at 300 K. The corresponding structures at the particular regions are also presented with some important bond lengths in Å. The  $\xi$  and  $x_{\perp}$  are in Å, while free energy surfaces are in kcal/mol.

The first path of the water adsorption reaction **r04** explores the effect of water on chemisorbed species with two interfacial Al–O bonds. A flat area on the reactant side is observed in Figure 8, which is exemplified by the **r04-(a)** and **r04-(b)** structures. While **r04-(a)** represents water weakly bound to the surface O2 atom by a hydrogen bond with a length of 1.8 Å, the water oxygen atom in **r04-(b)** is engaged in a nucleophilic attack on Al. At  $\xi \approx 0.5$ , pentacoordinated Al intermediates appear in **r04-(e)** and **r04-(f)**, which eventually induce methane desorption, as shown in **r04-(d)**. The unfavorable path via

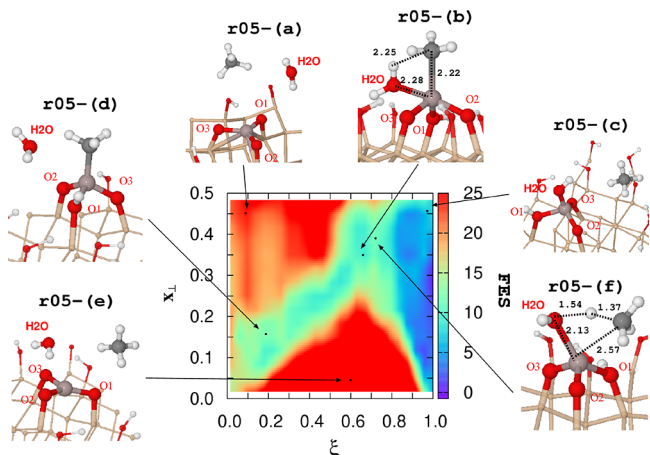


**Figure 9.** Two-dimensional free energy surface (FES) along reaction **r05** as obtained by neural net potential at 300 K. The corresponding structures at the particular regions are also presented with some important bond lengths in Å. The  $\xi$  and  $x_{\perp}$  are in Å, while free energy surfaces are in kcal/mol.

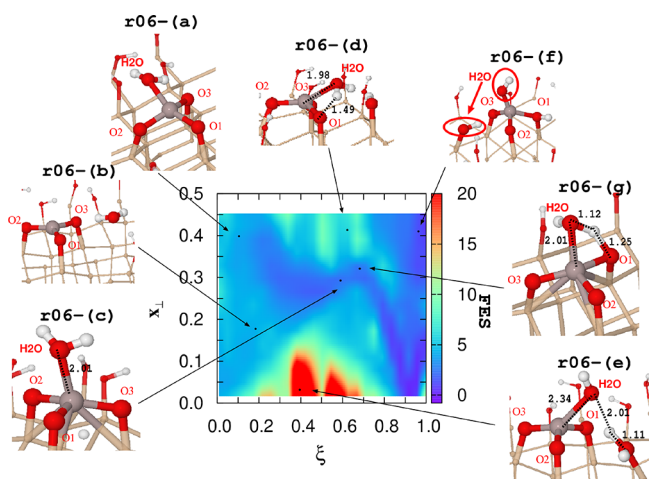


**Figure 10.** Two-dimensional free energy surface (FES) along reaction **r06** as obtained by neural net potential at 300 K. The corresponding structures at the particular regions are also presented with some important bond lengths in Å. The  $\xi$  and  $x_{\perp}$  are in Å, while free energy surfaces are in kcal/mol.

**r04-(c)** represents initial elimination of the methyl group because a much stretched Al–C2 = 2.54 Å is seen.

Unlike the path **r04** above, water adsorption on the chemisorbed Al with three interfacial Al–O bonds in **r05** results in a narrow channel of the reaction path, which is seen on the free energy surface in Figure 9. Along the reaction channel, the initial approach shown in **r05-(d)** results in a nucleophilic attack of Al by water oxygen in **r05-(b)**. Subsequently, the water hydrogen migrates to a methyl group in **r05-(f)** and eventually produces a methane and a tetracoordinated surface Al with a hydroxyl group in **r05-(c)**. As in the case of **r04**, the hydrogen attached to the methyl group originates from the incoming water molecule, rather than from the surface OH groups. The high-energy area exemplified by **r05-(a)** and **r05-(e)** represents the formation of methane before water adsorption. In these high-energy structures, the H atom consumed in  $\text{CH}_4$  comes from the surface rather than the incoming water. Hence, the incoming water provides for a more favorable methane formation than the surface OH groups.

In the case of **r06**, there is no methyl group in the tricoordinated Al. Therefore, the incoming water molecule initially approaches the electron-deficient Al as seen in **r06-(a)** and **r06-(b)**, which subsequently transfers a hydrogen to one of the surface oxygens in **r06-(d)** and **r06-(g)**. This produces a tetracoordinated Al and a hydroxyl group, as represented by **r06-(f)**. On the other hand, in the high-energy structure **r06-(e)**, a water hydrogen is transferred to a nearby surface hydroxyl group to produce surface adsorbed water.

**Temperature Effects.** A typical temperature range of ALD is rather wide, 300–600 K.<sup>6</sup> It seems important to determine an optimum range of temperatures for each different precursors. In order to study the effects of temperature on free energy surfaces, in addition to the 300 K simulations presented above, the NVT simulations at 600 K were also performed by ML-TDUS (machine learning with two-dimensional umbrella sampling) for the six reaction paths. The minimum free energy paths and the free energy barriers were located and are shown in Figure 11 and Table 1, respectively.

At 300 K, the methane desorption reactions of **r01**, **r02**, and **r03** proceed through reaction barriers of 3.03, 0.80, and 3.94 kcal/mol (see Table 1), respectively. The free energy barrier of 3.03 kcal/mol, which represents most of the initial physisorbed species (Figure 2a), implies that these species do not easily undergo subsequent surface chemical reactions. Therefore, the physisorbed species would be the main initial products.

This barrier height is reduced to 2.32 kcal/mol at 600 K, showing a substantial temperature effect of surface chemical reactions. Higher local temperatures can be achieved, e.g., with the use of precursors with high kinetic energy; this option will be discussed in the next section. Once the initial barrier is overcome, the formation of species with three interfacial Al–O bonds (Figure 2c) has a relatively low free energy barrier of 0.8 kcal/mol. However, the desorption of methane from these structures proceeds over a relatively large barrier of 3.94 kcal/mol.

In terms of the overall reaction free energy changes ( $\Delta G$ ), the methane desorption in **r01** has the largest free energy release and  $\Delta G$  values of **r02** and **r03** are smaller. For the first two reactions in Table 1,  $\Delta G$  at an elevated temperature becomes more negative. Therefore, the desorption of the first methane is preferred at higher temperatures, as both the reaction barrier and  $\Delta G$  decrease.

By contrast, the surface hydration (with methane desorption in the case of **r04** and **r05**) occurs nearly barrier-free (see the one-dimensional potential energy surface (free energy surface) in Figure 11). It should be emphasized that the hydrogen needed to form methane from the methyl group comes from the water molecule in **r04** and **r05**, while for **r01**, **r02**, and **r03**, it comes from the surface hydroxyl group. This shows that water has a significant catalytic effect for the desorption of methane. In general, **r04** and **r05** exhibit an exothermicity greater than 7.37–11.34 kcal/mol, while **r06** is less exothermic, mainly due to the missing  $\text{CH}_4$  evolution (See Table 1). In summary, precursor water is quite effective in removing the remaining surface methyl groups from the surface. In addition, water can easily restore the surface hydroxyl group. The initial adsorption of water on Al forms a penta- (**r04** and **r05**) and tetra- (**r06**) coordinated structures. This initial oversaturated coordination produces methane by breaking C–Al bonds in **r04** and **r05**.

Previously, on the OH/Si(100)-2X1 surface, the first-principles studies<sup>54,55</sup> predicted for **r01** an activation barrier of 11.53–16.6 kcal/mol, which is higher than that of **r02** (4.84–

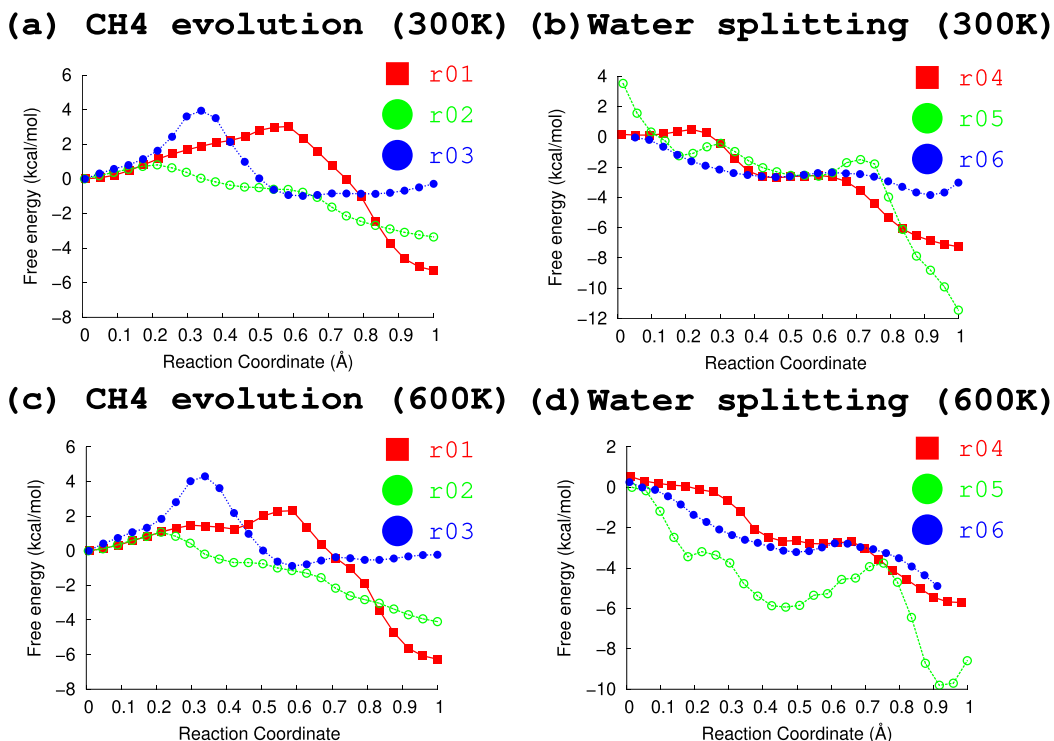


**Figure 11.** Free energy surfaces for  $\text{CH}_4$  evolution and water splitting reaction on surface TMA: (a) Free energy change of  $\text{CH}_4$  evolution at 300 K (red, green, and blue are the reaction labels r01, r02, and r03, respectively) (b) Free energy change of water splitting at 300 K (red, green, and blue are the reaction labels r04, r05, and r06). (c) Free energy change of  $\text{CH}_4$  evolution at 600 K (red, green, and blue are the reaction labels r01, r02, and r03, respectively) (d) Free energy change of water splitting at 600 K (red, green, and blue are the reaction labels r04, r05, and r06).

**Table 1. Summary of Activation Energy and Reaction Free Energy (in kcal/mol) for  $\text{CH}_4$  Evolution from Surface TMA**

label	$\Delta G$ (300 K)	$\Delta G$ (600 K)	$E^\ddagger$ (300 K)	$E^\ddagger$ (600 K)
r01	-5.29	-6.26	3.03	2.32
r02	-3.36	-4.09	0.80	1.07
r03	-0.87	-0.79	3.94	4.30
r04	-7.37	-6.26	N. A.	N. A.
r05	-11.34	-10.50	N. A.	N. A.
r06	-3.71	-4.88	N. A.	N. A.

12.9 kcal/mol). It should be noted that previous studies considered the methane desorption without formation of an additional interfacial Al–O bond. Furthermore, they were performed at the static structures, whereas the values obtained by ML-TDUS are the free energies, which explicitly include the entropy. However, the trend previously obtained that the barrier  $r01 > r02$  is consistent with the one obtained here. The higher initial barrier of r01 is also consistent with the recent experimental study<sup>21</sup> on the Si(111) and H/Si(111) surfaces, which showed that the reaction cross section of the initial TMA half cycle is generally lower than that of the TMA half cycle during the steady growth regime of ALD. In contrast, all  $\text{H}_2\text{O}$  half-cycles, including the first, were also shown to exhibit steady growth behavior, which is consistent with our nearly barrier-free surface hydration.

Various stages of reactions of r01–r06 indicate multiple intermediates with a wide range of their kinetic stability. Perhaps, such diverse possibilities can produce a heterogeneous surface morphology. The consequences of this could be confirmed by experimental observation of water-stable methyl species<sup>25</sup> or retention of hydroxyl groups as a source of hydrogen content.<sup>22</sup>

**Adsorption Dynamics.** The free energy surfaces presented above for the surface chemical reactions after the initial physisorption revealed finer details of the surface reactions as compared to the static potential energy surfaces. However, the FES (free energy surface) does not show the kinetic aspects of the initial contact process. The kinetics can be revealed in molecular dynamics simulations (Figure 12).

Although using the monomer TMA in computational studies has been a standard practice, its dimer ( $\text{Al}_2\text{Me}_6$ ) is commonly formed in the gas phase. The nucleophilic attack of one of the Al atoms by surface oxygen can easily break the bridging methyl, restoring the initial chemisorption (Figure 2a). Therefore, the expected effect of the dimer can be relatively small. Nevertheless, the effect of the dimer on overall "absorption dynamics" needs to be studied in the future.

The adsorption probabilities as well as the initial surface product types were simulated in a range of  $u_{\text{rms}}$  values, and the results are presented in Figure 13. The root mean square velocity ( $u_{\text{rms}}$ ) of the TMA gas at 300 K is 3.22 Å/ps. At this velocity, the probability of occurrence of RM1 and R0 are ca. 60 and 40%, respectively, which means that only ca. 40% of the initial contacts successfully form the physisorbed surface product as shown in Figure 13a. The maximum probability of physisorption (R0) of ca. 70% was achieved at  $u_{\text{rms}} = 15\text{--}20$  Å/ps. However, the probability of physisorption quickly drops at a higher velocity ( $u_{\text{rms}} > 20$  Å/ps) and is accompanied by a minor increase in the surface populations of R01 and R02.

For a number of  $u_{\text{rms}}$  values, a distribution of the simulation times at which the Al–O bond formation occurs is shown in Figure 13b. A broader distribution of successful contact times occurs at a lower velocity (red), although the successful formation probability is relatively low during the entire contact

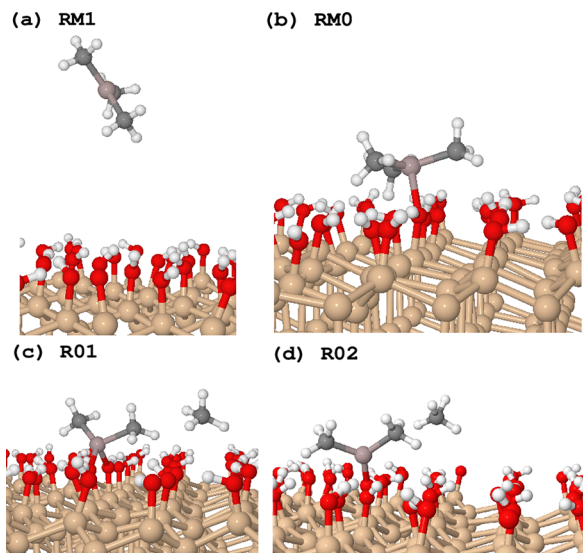


**Figure 12.** Summary of initial TMA reaction: (a) Geometry of reaction products, RM1: TMA does not attach to the surface, R0: TMA attaches to the surface without CH<sub>4</sub> release, R01: TMA attaches to the surface with two Al–O bonds and releases one CH<sub>4</sub>, and R02: TMA attaches to the surface with one Al–O bond and releases one CH<sub>4</sub>.

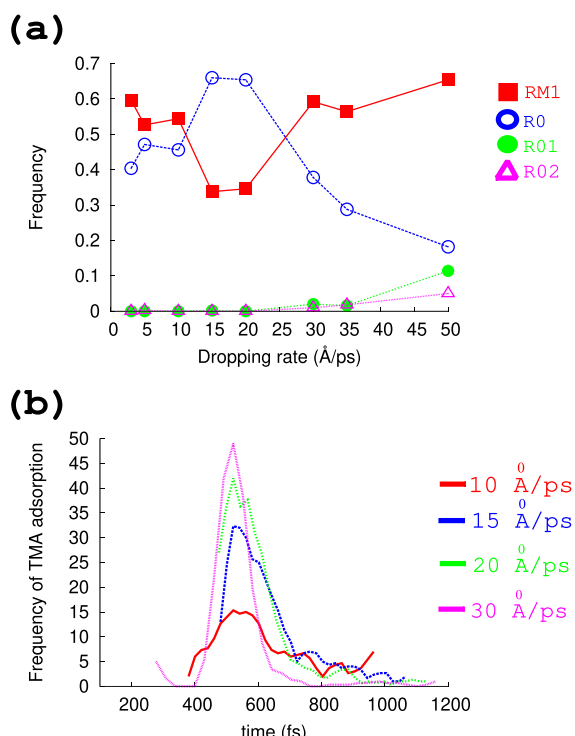


**Figure 13.** Summary of the initial TMA reaction at varying dropping rate: (a) Probability of the respective product of initial TMA contact. Red, blue, green, and magenta denote RM1, R0, R01, and R02, respectively. Horizontal axis denotes the dropping rate, and the vertical axis shows the probability to obtain the respective product. RM1: TMA does not attach to the surface, RM0: TMA attaches to the surface without CH<sub>4</sub> release, R01: TMA attaches to the surface with two Al–O bonds and releases one CH<sub>4</sub>, and R02: TMA attaches to the surface with one Al–O bond and releases one CH<sub>4</sub>. (b) Histogram showing the time of formation of the initial Al–O bond. Red, blue, green, and magenta denote 10, 15, 20, and 30 Å/ps, respectively.

time. On the other hand, a very large successful contact ratio at around 550 fs is seen at high velocity (magenta). However, successful contacts occur only within a narrow range of simulation times.

As a result, the maximum probability of physisorption in Figure 13a can be attributed to a tradeoff between the width of the successful contact time (or the resident time on the surface) and the magnitude of the kinetic energy. At a faster  $u_{\text{rms}}$  velocity (above 35 Å/ps), both R01 and R02 start to appear.

It can be expected that different regions on the surface of OH-Si(111) have different propensities to adsorption. To examine the relative reactivity of the surface regions, a distribution of the successful adsorption events with respect to a particular surface region is plotted in Figure 14a and the corresponding surface

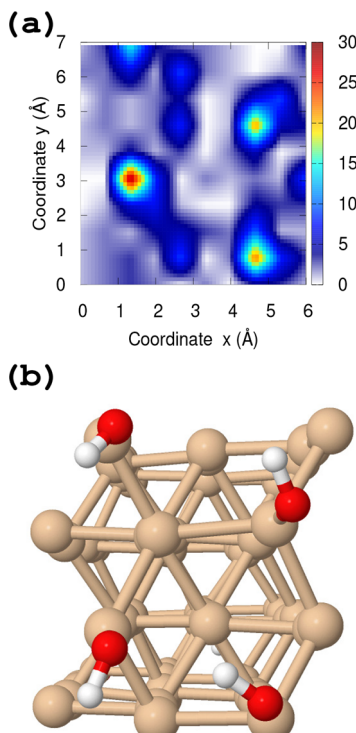


**Figure 14.** (a) Number of successful TMA adsorption events per each atomic site at  $u_{\text{rms}} = 15$  Å/ps. (b) Corresponding geometry of surface OH-(111)Si.

structures are shown in Figure 14b. A strong correlation between the position of the surface OH groups and a high adsorption rate is seen in the figures. Therefore, the initial contact position of TMA on the surface is one of the determining factors for a successful adsorption.

## CONCLUSIONS

The recently developed low-dimensional projection technique (TDUS) was adopted for the ML training process to establish a protocol to obtain the most relevant training dataset. Here, we propose an iterative training procedure, with the training dataset gradually increasing at each iteration. The training process is terminated when convergence of the free energy surfaces generated by ML-TDUS below certain threshold is reached. The proposed ML-TDUS algorithm significantly (more than 100 times) reduces the computational burden of training the ML potentials.

When applying ML-TDUS to the ALD of Al(Me)<sub>3</sub> and water on the surface of the OH/Si(111),<sup>6</sup> the target free energy RMSE converges below 1.0 kcal/mol in as little as 8 iterations. The resulting free-energy landscapes of ML-TDUS revealed a number of new surface states and a variety of reaction pathways, which could not be discovered by static quantum-mechanical computations. Numerous surface proton transfer reactions, zwitterionic surface configuration, elimination–addition/addition–elimination reactions, S<sub>N</sub>2 reactions, and surface entropic and temperature effects have been discovered from the analysis of the free energy surfaces represented in a two-dimensional space of optimally selected collective variables.

In general, the S<sub>N</sub>2-type surface chemical reactions have reduced free energy barriers and are preferred before other types of surface reactions. According to the lowest free energy barriers of the minimum energy paths, the rate-limiting step upon the initial Al(Me)<sub>3</sub> adsorption is the methane desorption, which requires the highest activation free energy at 300 K. However, methane desorption is slightly facilitated at elevated temperatures. It is also found that the desorption of methane is considerably facilitated by water adsorption, which easily replaces surface methyl with the hydroxyl group.

Using the same ML-TDUS model, adsorption dynamics simulations were performed and showed that only 40% of the initial contacts successfully form the physisorbed surface product at 300 K. Maximum physisorption (R0) of *ca.* 70% was achieved with  $u_{rms} = 15\text{--}20 \text{ \AA}/\text{ps}$ . However, the probability of physisorption quickly drops at a higher velocity ( $u_{rms} > 20 \text{ \AA}/\text{ps}$ ). Therefore, the MD simulations reveal the existence of an optimal contact velocity of the incoming Al(Me)<sub>3</sub>, which maximizes the successful adsorption rate. On the basis of the same data, dependence of the successful contact rate on particular surface adsorption sites was discovered.

It has been also demonstrated that ML-TDUS is a very efficient protocol, which can be used to study complex chemical reaction dynamics at a much reduced computational cost. Its application to the Al(Me)<sub>3</sub>/H<sub>2</sub>O ALD process revealed several interesting findings, which could otherwise be extremely difficult to obtain using *ab initio* static computations only.

## ASSOCIATED CONTENT

### Supporting Information

The Supporting Information is available free of charge at <https://pubs.acs.org/doi/10.1021/acsami.2c01768>.

Tables S1 and S2: Detailed description of reaction coordinate for each CH<sub>4</sub> evolution, and water; Figures S1 and S2: Detailed comparison between density functional theory and the ML force field ([PDF](#))

## AUTHOR INFORMATION

### Corresponding Authors

Hiroya Nakata – Department of Chemistry, Kyungpook National University, Daegu 41566, South Korea;  
Email: [nakata.hiro07@gmail.com](mailto:nakata.hiro07@gmail.com)

Michael Filatov(Gulak) – Department of Chemistry, Kyungpook National University, Daegu 41566, South Korea;  
[orcid.org/0000-0002-1541-739X](https://orcid.org/0000-0002-1541-739X); Email: [mike.filatov@gmail.com](mailto:mike.filatov@gmail.com)

Cheol Ho Choi – Department of Chemistry, Kyungpook National University, Daegu 41566, South Korea;  
[orcid.org/0000-0002-8757-1396](https://orcid.org/0000-0002-8757-1396); Email: [cchoi@knu.ac.kr](mailto:cchoi@knu.ac.kr)

Complete contact information is available at:  
<https://pubs.acs.org/10.1021/acsami.2c01768>

### Author Contributions

H.N. performed all calculations and initial analysis. M.F. improved the main texts and performed an additional analysis. C.H.C. designed the project, analyzed data, and wrote the manuscript.

### Notes

The authors declare no competing financial interest.

## ACKNOWLEDGMENTS

We thank Dr. Taek-Mo Chung at the Korea Research Institute of Chemical Technology for his invaluable discussion. This work was supported by the Samsung Science and Technology Foundations (SSTF-BA1701-12) for the fundamental theory developments and the NRF funded by the Ministry of Science and ICT (2020R1A2C2008246 and 2020R1A5A1019141). It is also supported by the Korea Polar Research Institute (KOPRI, PE21120).

## REFERENCES

- (1) George, S. M. Atomic Layer Deposition: An Overview. *Chem. Rev.* **2010**, *110*, 111–131. PMID: 19947596
- (2) Johnson, R. W.; Hultqvist, A.; Bent, S. F. A Brief Review of Atomic Layer Deposition: From Fundamentals to Applications. *Mater. Today* **2014**, *17*, 236–246.
- (3) Oviroh, P. O.; Akbarzadeh, R.; Pan, D.; Coetzee, R. A. M.; Jen, T.-C. New Development of Atomic Layer Deposition: Processes, Methods and Applications. *Science and Technology of Advanced Materials* **2019**, *20*, 465–496. PMID: 31164953,
- (4) Gakis, G. P.; Vahlas, C.; Vergnes, H.; Dourdain, S.; Tison, Y.; Martinez, H.; Bour, J.; Ruch, D.; Boudouvis, A. G.; Caussat, B.; et al. Investigation of the Initial Deposition Steps and the Interfacial Layer of Atomic Layer Deposited (ALD) Al<sub>2</sub>O<sub>3</sub> on Si. *Appl. Surf. Sci.* **2019**, *492*, 245–254.
- (5) Sheng, J.; Lee, J.-H.; Choi, W.-H.; Hong, T.; Kim, M.; Park, J.-S. Review Article: Atomic Layer Deposition for Oxide Semiconductor Thin Film Transistors: Advances in Research and Development. *Journal of Vacuum Science & Technology A* **2018**, *36*, No. 060801.
- (6) Puurunen, R. L. Surface Chemistry of Atomic Layer Deposition: A Case Study for the Trimethylaluminum/water Process. *J. Appl. Phys.* **2005**, *97*, 121301.
- (7) Ye, P. D.; Wilk, G. D.; Kwo, J.; Yang, B.; Gossmann, H. J.; Frei, M.; Chu, S. N.; Mannaerts, J. P.; Sergeant, M.; Hong, M. et al. *GaAs MOSFET with Oxide Gate Dielectric Grown by Atomic Layer Deposition*. 2003.
- (8) Klein, T. M.; Niu, D.; Epling, W. S.; Li, W.; Maher, D. M.; Hobbs, C. C.; Hegde, R. I.; Baumvol, I. J.; Parsons, G. N. Evidence of Aluminum Silicate Formation During Chemical Vapor Deposition of Amorphous Al<sub>2</sub>O<sub>3</sub> Thin Films on Si(100). *Appl. Phys. Lett.* **1999**, *75*, 4001.
- (9) Manchanda, L.; Morris, M. D.; Green, M. L.; Van Dover, R. B.; Klemens, F.; Sorsch, T. W.; Silverman, P. J.; Wilk, G.; Busch, B.; Aravamudhan, S. Multi-component High-K Gate Dielectrics for the Dilicon Industry. *Microelectron. Eng.* **2001**, *59*, 351.
- (10) Ritala, M.; Saloniemi, H.; Leskelä, M.; Prohaska, T.; Friedbacher, G.; Grasserbauer, M. Studies on the Morphology of Al<sub>2</sub>O<sub>3</sub> Thin Films Grown by Atomic Layer Epitaxy. *Thin Solid Films* **1996**, *286*, 54.
- (11) Yates, D. J.; Dembinski, G. W.; Kroll, W. R.; Elliott, J. J. Infrared Studies of the Reactions Between Silica and Trimethylaluminum. *J. Phys. Chem.* **1969**, *73*, 911.
- (12) Kukli, K.; Ritala, M.; Leskelä, M.; Jokinen, J. Atomic Layer Epitaxy Growth of Aluminum Oxide Thin Films from a Novel Al(CH<sub>3</sub>)<sub>2</sub>Cl Precursor and H<sub>2</sub>O. *J. Vac. Sci. Technol., A* **1997**, *15*, 2212.

- (13) Huang, R.; Kitai, A. H. Preparation and Characterization of Thin Films of MgO, Al<sub>2</sub>O<sub>3</sub> and MgAl<sub>2</sub>O<sub>4</sub> by Atomic Layer Deposition. *J. Electron. Mater.* **1993**, *22*, 215–220.
- (14) Hiltunen, L.; Kattelus, H.; Leskelä, M.; Mäkelä, M.; Niinistö, L.; Nykänen, E.; Soininen, P.; Tiittad, M. Growth and Characterization of Aluminium Oxide Thin Films Deposited from Various Source Materials by Atomic Layer Epitaxy and Chemical Vapor Deposition Processes. *Mater. Chem. Phys.* **1991**, *28*, 379.
- (15) Widjaja, Y.; Musgrave, C. B. Quantum Chemical Study of the Mechanism of Aluminum Oxide Atomic Layer Deposition. *Appl. Phys. Lett.* **2002**, *80*, 3304.
- (16) Heyman, A.; Musgrave, C. B. A Quantum Chemical Study of the Atomic Layer Deposition of Al<sub>2</sub>O<sub>3</sub> Using AlCl<sub>3</sub> and H<sub>2</sub>O as Precursors. *J. Phys. Chem. B* **2004**, *108*, 5718.
- (17) Halls, M. D.; Raghavachari, K. Atomic Layer Deposition Growth Reactions of Al<sub>2</sub>O<sub>3</sub> on Si(100)-2Å-1. *J. Phys. Chem. B* **2004**, *108*, 4058.
- (18) Lee, S. S.; Baik, J. Y.; An, K. S.; Suh, Y. D.; Oh, J. H.; Kim, Y. Reduction of Incubation Period by Employing OH-terminated Si(001) Substrates in the Atomic Layer Deposition of Al<sub>2</sub>O<sub>3</sub>. *J. Phys. Chem. B* **2004**, *108*, 15128.
- (19) Ghosh, M. K.; Choi, C. H. The Initial Mechanisms of Al<sub>2</sub>O<sub>3</sub> Atomic Layer Deposition on OH/Si(1 0 0)-2 Å-1 Surface by Trimethylaluminum and Water. *Chem. Phys. Lett.* **2006**, *426*, 365–369.
- (20) Kinnunen, S.; Arstila, K.; Sajavaara, T. Al<sub>2</sub>O<sub>3</sub> ALD Films Grown Using TMA + Rare Isotope 2H<sub>2</sub>16O and 1H<sub>2</sub>18O Precursors. *Appl. Surf. Sci.* **2021**, *546*, No. 148909.
- (21) Vandalon, V.; Erwin Kessels, W. M. Initial Growth Study of Atomic-Layer Deposition of Al<sub>2</sub>O<sub>3</sub> by Vibrational Sum-Frequency Generation. *Langmuir* **2019**, *35*, 10374–10382.
- (22) Guerra-Nuñez, C.; Döbeli, M.; Michler, J.; Utke, I. Reaction and Growth Mechanisms in Al<sub>2</sub>O<sub>3</sub> Deposited via Atomic Layer Deposition: Elucidating the Hydrogen Source. *Chem. Mater.* **2017**, *29*, 8690–8703.
- (23) Batra, N.; Gope, J.; Panigrahi, J.; Singh, R.; Singh, P. K. Influence of Deposition Temperature of Thermal ALD Deposited Al<sub>2</sub>O<sub>3</sub> Films on Silicon Surface Passivation. *AIP Adv.* **2015**, *5*, 67113.
- (24) Werbrouck, A.; Shirazi, M.; Mattelaer, F.; Elliott, S. D.; Dendooven, J.; Detavernier, C. A Secondary Reaction Pathway for the Alumina Atomic Layer Deposition Process with Trimethylaluminum and Water, Revealed by Full-Range, Time-Resolved *In Situ* Mass Spectrometry. *J. Phys. Chem. C* **2020**, *124*, 26443–26454.
- (25) Jin, Z.; Lee, S.; Shin, S.; Shin, D.-S.; Choi, H.; Min, Y.-S. Chemical Probing of Water-Stable Methyl Species in Atomic Layer Deposition of Al<sub>2</sub>O<sub>3</sub> from Trimethylaluminum and Water. *J. Phys. Chem. C* **2021**, *125*, 21434–21442.
- (26) Chen, L.; Warburton, R. E.; Chen, K.-S.; Libera, J. A.; Johnson, C.; Yang, Z.; Hersam, M. C.; Greeley, J. P.; Elam, J. W. Mechanism for Al<sub>2</sub>O<sub>3</sub> Atomic Layer Deposition on LiMn<sub>2</sub>O<sub>4</sub> from *In Situ* Measurements and Ab Initio Calculations. *Chem* **2018**, *4*, 2418–2435.
- (27) Behler, J. Constructing High-Dimensional Neural Network Potentials: A tutorial review. *Int. J. Quantum Chem.* **2015**, *115*, 1032–1050.
- (28) Bartók, A. P.; Payne, M. C.; Kondor, R.; Csányi, G. Gaussian Approximation Potentials: The Accuracy of Quantum Mechanics, without the Electrons. *Phys. Rev. Lett.* **2010**, *104*, No. 136403.
- (29) Chmiela, S.; Tkatchenko, A.; Sauceda, H. E.; Poltavsky, I.; Schütt, K. T.; Müller, K.-R. Machine Learning of Accurate Energy-Conserving Molecular Force Fields. *Sci. Adv.* **2017**, *3*, No. e1603015.
- (30) Zhang, L.; Han, J.; Wang, H.; Car, R.; Weinan, E. Deep Potential Molecular Fynamics: a Dcalable Model with the Accuracy of Quantum Mechanics. *Phys. Rev. Lett.* **2018**, *120*, No. 143001.
- (31) Wang, H.; Zhang, L.; Han, J.; Weinan, E. DeePMD-kit: A Deep Learning Package for Many-Body Potential Energy Representation and Molecular Dynamics. *Comput. Phys. Commun.* **2018**, *228*, 178–184.
- (32) Zhou, Y.; Wang, S.; Zhang, Y. Catalytic Reaction Mechanism of Acetylcholinesterase Determined by Born- Oppenheimer Ab Initio QM/MM Molecular Dynamics Simulations. *J. Phys. Chem. B* **2010**, *114*, 8817–8825.
- (33) Yang, M.; Yang, L.; Gao, Y.; Hu, H. Combine Umbrella Sampling with Integrated Tempering Method for Efficient and Accurate Calculation of Free Energy Changes of Complex Energy Surface. *J. Chem. Phys.* **2014**, *141*, 07B618\_1.
- (34) Uddin, N.; Choi, T. H.; Choi, C. H. Direct Absolute p K a Predictions and Proton Transfer Mechanisms of Small Molecules in Aqueous Solution by QM/MM-MD. *J. Phys. Chem. B* **2013**, *117*, 6269–6275.
- (35) Baek, Y. S.; Choi, C. H. One-Dimensional Projection of Collective Variables for Effective Sampling of Complex Chemical Reaction Coordinates. *J. Chem. Theory Comput.* **2018**, *14*, 2312–2321.
- (36) Kästner, J.; Senn, H. M.; Thiel, S.; Otte, N.; Thiel, W. QM/MM Free-Energy Perturbation Compared to Thermodynamic Integration and Umbrella Sampling: Application to an enzymatic reaction. *J. Chem. Theory Comput.* **2006**, *2*, 452–461.
- (37) Futera, Z.; Burda, J. V. Reaction Mechanism of Ru (II) Piano-Dtool Vomplexes: Umbrella Dampling QM/MM MD Study. *J. Comput. Chem.* **2014**, *35*, 1446–1456.
- (38) Fedorov, D. G.; Sugita, Y.; Choi, C. H. Efficient Parallel Implementations of QM/MM-REMD (Quantum Mechanical/Molecular Mechanics-Replica-Exchange MD) and Umbrella Sampling: Isomerization of H<sub>2</sub>O<sub>2</sub> in Aqueous Solution. *J. Phys. Chem. B* **2013**, *117*, 7996–8002.
- (39) Raiteri, P.; Laio, A.; Gervasio, F. L.; Micheletti, C.; Parrinello, M. Efficient Reconstruction of Complex Free Energy Landscapes by Multiple Walkers Metadynamics. *J. Phys. Chem. B* **2006**, *110*, 3533–3539.
- (40) Laio, A.; Gervasio, F. L. Metadynamics: a Method to Simulate Rare Events and Reconstruct the Free Energy in Biophysics. *Rep. Prog. Phys.* **2008**, *71*, No. 126601.
- (41) Bussi, G.; Gervasio, F. L.; Laio, A.; Parrinello, M. Free-Energy Landscape for β Hairpin Folding from Combined Parallel Tempering and Metadynamics. *J. Am. Chem. Soc.* **2006**, *128*, 13435–13441.
- (42) Iino, T.; Sakurai, M.; Furuta, T. A Novel Ring-Shaped Reaction Pathway with Interconvertible Intermediates in Chitinase A as Revealed by QM/MM Simulation Combined with a One-Dimensional Projection Technique. *Phys. Chem. Chem. Phys.* **2019**, *21*, 24956–24966.
- (43) Nakata, H.; Choi, C. H. Low-Dimensional Projection Approach for Efficient Sampling of Molecular Recognition and Polymer Aggregation. *Phys. Chem. Chem. Phys.* **2020**, *22*, 6953–6963.
- (44) Plimpton, S. Fast Parallel Algorithms for Short-Range Molecular Dynamics. *J. Comput. Phys.* **1995**, *117*, 1–19.
- (45) Artacho, E.; Anglada, E.; Diéguez, O.; Gale, J. D.; García, A.; Junquera, J.; Martín, R. M.; Ordejón, P.; Pruneda, J. M.; Sánchez-Portal, D.; et al. The SIESTA Method. Developments and Applicability. *J. Phys.: Condens. Matter* **2008**, *20*, No. 064208.
- (46) Sánchez-Portal, D.; Ordejón, P.; Canadell, E. *Principles and Applications of Density Functional Theory in Inorganic Chemistry II*; Springer, 2004; pp. 103–170, DOI: 10.1007/b97943.
- (47) Hammouri, M.; Jha, S. K.; Vasiliev, I. First-principles Study of Graphene and Carbon Nanotubes Functionalized with Benzyne. *J. Phys. Chem. C* **2015**, *119*, 18719–18728.
- (48) Perdew, J. P.; Burke, K.; Ernzerhof, M. Generalized Gradient Approximation Made Simple. *Phys. Rev. Lett.* **1996**, *77*, 3865–3868.
- (49) Perdew, J. P.; Burke, K.; Ernzerhof, M. Generalized Gradient Approximation Made Simple. *Phys. Rev. Lett.* **1997**, *78*, 1396.
- (50) Hamann, D.; Schlüter, M.; Chiang, C. Norm-Conserving Pseudopotentials. *Phys. Rev. Lett.* **1979**, *43*, 1494.
- (51) Monkhorst, H. J.; Pack, J. D. Special Points for Brillouin-Zone Integrations. *Phys. Rev. B* **1976**, *13*, 5188.
- (52) Nosé, S. A Molecular Dynamics Method for Simulations in the Canonical Ensemble. *Mol. Phys.* **1984**, *52*, 255–268.
- (53) Nosé, S. A Unified Formulation of the Constant Temperature Molecular Dynamics Methods. *J. Chem. Phys.* **1984**, *81*, 511–519.
- (54) Ghosh, M. K.; Choi, C. H. Adsorption Reactions of Dimethylaluminum Isopropoxide and Water on the H/Si(100)-2 x 1 Surface: Initial Reactions for Atomic Layer Deposition of Al<sub>2</sub>O<sub>3</sub>. *J. Phys. Chem. B* **2006**, *110*, 11277–11283.

- (55) Kim, D.-H.; Baek, S.-B.; Seo, H.-I.; Kim, Y.-C. Interactions Between Tri-Methylaluminum Molecules and Their Effect on the Reaction of Tri-methylaluminum with an OH-terminated Si (0 0 1) Surface. *Appl. Surf. Sci.* **2011**, *257*, 6326–6331.
- (56) Andrade, M. F. C.; Ko, H.-Y.; Zhang, L.; Car, R.; Selloni, A. Free Energy of Proton Transfer at the Water–TiO<sub>2</sub> Interface from Ab Initio Deep Potential Molecular Dynamics. *Chem. Sci.* **2020**, *11*, 2335–2341.
- (57) Bonati, L.; Parrinello, M. Silicon Liquid Structure and Crystal Nucleation from Ab Initio Deep Metadynamics. *Phys. Rev. Lett.* **2018**, *121*, No. 265701.
- (58) Quaranta, V.; Hellström, M.; Behler, J. Proton-Transfer Mechanisms at the Water–ZnO Interface: The Role of Presolvation. *J. Phys. Chem. Lett.* **2017**, *8*, 1476–1483.
- (59) Yang, M.; Bonati, L.; Polino, D.; Parrinello, M. Using Metadynamics to Build Neural Network Potentials for Reactive Events: the Case of Urea Decomposition in Water. *Catal. Today* **2022**, *387*, 143.
- (60) Zeng, J.; Cao, L.; Xu, M.; Zhu, T.; Zhang, J. Z. Complex Reaction Processes in Combustion Unraveled by Neural Network-Based Molecular Dynamics simulation. *Nat. Commun.* **2020**, *11*, 1–9.

## □ Recommended by ACS

### Robust, Multi-Length-Scale, Machine Learning Potential for Ag–Au Bimetallic Alloys from Clusters to Bulk Materials

Christopher M. Andolina, Wissam A. Saidi, *et al.*

JULY 29, 2021

THE JOURNAL OF PHYSICAL CHEMISTRY C

READ ▶

### Active Learning the Potential Energy Landscape for Water Clusters from Sparse Training Data

Troy D. Loeffler, Subramanian K. R. S. Sankaranarayanan, *et al.*

JANUARY 31, 2020

THE JOURNAL OF PHYSICAL CHEMISTRY C

READ ▶

### Machine Learning-Guided Approach for Studying Solvation Environments

Yasemin Basdogan, John A. Keith, *et al.*

DECEMBER 06, 2019

JOURNAL OF CHEMICAL THEORY AND COMPUTATION

READ ▶

### Toward *ab Initio* Ground States of Gold Clusters via Neural Network Modeling

Aidan Thorn, Aleksey N. Kolmogorov, *et al.*

NOVEMBER 25, 2019

THE JOURNAL OF PHYSICAL CHEMISTRY C

READ ▶

Get More Suggestions >